Article

Pore Morphology Determines Spontaneous Liquid Extrusion from Nanopores

Matteo Amabili, Yaroslav Grosu, Alberto Giacomello, Simone Meloni, Abdelali Zaki, Francisco Bonilla, Abdessamad Faik, and Carlo Massimo Casciola

ACS Nano, **Just Accepted Manuscript** • DOI: 10.1021/acsnano.8b07818 • Publication Date (Web): 17 Jan 2019

Pore Morphology Determines Spontaneous Liquid Extrusion from Nanopores

Matteo Amabili,[†] Yaroslav Grosu,[‡] Alberto Giacomello,[*,†] Simone Meloni,[*,†] Abdelali Zaki,[‡] Francisco Bonilla,[‡] Abdessamad Faik,[‡] and Carlo Massimo Casciola[†]

[†]*Sapienza Università di Roma, Dipartimento di Ingegneria Meccanica e Aerospaziale, 00184 Rome, Italy*

[‡]*CIC Energigune, Albert Einstein 48, Miñano (Álava) 01510, Spain*

E-mail: alberto.giacomello@uniroma1.it; simone.meloni@uniroma1.it

Phone: +39 06 44585200

Abstract

In this contribution we explore by means of experiments, theory, and molecular dynamics the effect of pore morphology on the spontaneous extrusion of non-wetting liquids from nanopores. Understanding and controlling this phenomenon is central for manipulating nanoconfined liquids, *e.g.*, in nanofluidic applications, drug delivery, and oil extraction. Qualitatively different extrusion behaviors were observed in high-pressure water intrusion-extrusion experiments on porous materials with similar nominal diameter and hydrophobicity: macroscopic capillary models and molecular dynamics simulations revealed that the very presence or absence of extrusion is connected to the internal morphology of the pores and, in particular, to the presence of small-scale roughness or pore interconnections. Additional experiments with mercury confirmed that this mechanism is generic for non-wetting liquids and is rooted in the

pore topology. The present results suggest a rational way to engineer heterogeneous systems for energy and nanofluidic applications in which the extrusion behavior can be controlled *via* the pore morphology.

Keywords

nanoporous materials, liquid extrusion, surface roughness, hydrophobicity, molecular dynamics

Liquids confined in nanoporous materials often display peculiar behaviors which are exploited in a broad range of nanofluidic and energy applications. A paradigmatic example is represented by heterogeneous lyophobic systems (HLSs) formed by a nanoporous material immersed in a non-wetting liquid; this rapidly growing research field focuses on the intrusion and extrusion behavior of HLS for energy storage[1–6] and energy dissipation[7,8] with the final goal of engineering this class of materials. In HLS, mechanical energy is stored in the form of liquid-solid interfacial energy during the high-pressure intrusion of a liquid (often water) into the lyophobic porous material. The pressure at which the liquid spontaneously extrudes from the pores (discharge) defines the applicability of HLS: if extrusion takes place at pressures comparable to the intrusion one[3,9] HLS is suitable for energy storage (*molecular spring* behavior). If, instead, the extrusion pressure is considerably lower than the intrusion one[6,7,10,11] (pressure hysteresis) HLS can be used to dissipate energy, *e.g.*, mechanical vibrations (*damper* behavior) under repeated intrusion-extrusion cycles. Finally, if the non-wetting liquid remains trapped in the pores even when the pressure is lowered down to the minimum working value,[12] HLS can be used for dissipating the energy of a single impact (*bumper* behavior).

The ultrahigh surface areas per gram typical of nanoporous materials,[13,14] together with the high surface tension of water, make such systems more compact and effective as compared to conventional technologies both for energy storage and for vibration damping. For example, a car shock absorber based on HLS, where {water + grafted silica} is used as a work-

ing medium, outperforms conventional oil-based shock absorber in several important ways. First of all, the energy capacity is considerably higher due to the fact that HLS-based shock absorbers do not require cumbersome springs to decompress them after the impact. High specific dissipation power of up to 50 W/cm^3 was reported for an HLS-based shock absorber.[11] Secondly, HLS-based shock absorbers are significantly more environmental-friendly as the amount of oil used is negligible as compared to oil-based shock absorber.[8,11,15] Finally, HLS-based shock absorber can withstand exceptional frequencies of compression-decompression cycling.[11,16,17] On the other hand, many applications based on HLSs are far behind, mainly because of the limited knowledge of pressure hysteresis – the difference between intrusion and extrusion pressures – and of the strategies to control it.

The aforementioned cases illustrate how pressure hysteresis determines the use of HLSs. Notwithstanding its technological relevance, the design of systems with controlled pressure hysteresis remains a challenge due to the lack of predictive theories. It is known that both the intrusion and extrusion pressures depend on the chemistry and on the geometry of the pores,[3,6,9,14,18] suggesting a route to control these phenomena. This insight is in agreement with the vast corpus focusing on the hydrophobic effect which has demonstrated that, in a variety of geometries, the formation of a confined vapor phase analogous to extrusion is facilitated by hydrophobic cavities;[19–30] such drying phenomena are of importance in diverse fields, including solution chemistry, protein folding, superhydrophobicity, *etc.* However, while for the intrusion pressure Laplace's law,[2,4,31] with nanoscale deviations for the smallest pores,[32] is known to work, for extrusion a comprehensive theory is still lacking in complex geometries. This lack of a quantitative understanding severely limits the exploitation of nanoconfined liquids in applications: for instance, rationalizing the early suggestion that bubbles within the pores facilitate pore dewetting[33] could lead to improved strategies to control the pressure hysteresis of HLS.

The aim of the present paper is to understand what are the characteristics of a porous material determining its extrusion behavior and to suggest flexible strategies to control the

phenomenon. In particular, we focus on two commercial porous materials with similar pore sizes and chemistry but whose internal features – pore interconnections or roughness of the internal surface – significantly differ. Our experiments show that these materials have qualitatively different behavior for what concerns water extrusion: in one case, the liquid is forced out of the pores at pressures as large as few megapascals while, in the other case, it does not extrude even when the pressure is decreased down to ambient pressure. In order to understand the origin of this qualitative difference, we employ models of pores which account for the essential topology of the two materials: one with independent pores and one with interconnected ones. We consider an increasing degree of sophistication for the behavior of water and for the solid-liquid interaction: a macroscopic capillarity model and a fully atomistic one; in the latter, mesoscale and nanoscale effects such as disjoining pressure, line tension, Tolman corrections, *etc.* are accounted for by the interatomic potentials without the need of ad-hoc models. First, in section *Extrusion: Theory*, the macroscopic model suggests that pore interconnections are a plausible explanation of extrusion in HLS. Secondly, in section *Extrusion: Molecular Dynamics*, atomistic simulations confirm that extrusion can be induced by internal roughness: free-energy calculations show a significant reduction of the extrusion free-energy barrier compatible with the extrusion time recorded in experiments. Additional *in silico* intrusion-extrusion experiments substantiate our explanation in pressure cycles. In the final section before conclusions, we demonstrate experimentally that the findings obtained with water are general and apply also to the case of other non-wetting liquids and different porous materials.

Summarizing, by combining experiments, macroscopic theory, and atomistic simulation, this work elucidates the role of nanoscale surface roughness or pore interconnections on the extrusion of liquids from nanoporous materials. The present results are valuable not only to further the development of HLSs but also of a broad variety of applications where the control of the behavior of nanoconfined liquids is essential.

Results and discussion

Experiments

The aim of the present experiments is to reveal the effect of pore topology on the intrusion-extrusion pressure hysteresis. For this purpose, two hydrophobic porous materials with similar pore sizes but different internal morphologies were subjected to high-pressure intrusion-extrusion experiments with water as the working liquid. Both materials –RPB and WC8– were commercial silica gels grafted with a hydrophobic coating following the same protocol (see also the *Methods* section for further details on the materials). The resulting surface chemistries are characterized by the same (apparent) contact angle as measured from compacted silica pellets (see the *Supporting Information*, Fig. SI1).

As a preliminary step, the two materials were characterized by TEM and SEM. The TEM micrographs in Figs. 1a and b show that the topology of the pores is very different for the two materials: RPB is characterized by independent pores with an approximately cylindrical shape while WC8 by randomly intersecting spheres. The disordered distribution of the latter pores results in a network of spherical cages interconnected by interstices having size less than the cage diameter, *i.e.*, less than ca. 10 nm. The SEM micrographs in the *Supporting Information*, Fig. SI2a-b, confirm that the cavity mouth of WC8 is of the order of 10 nm, but is inconclusive for RPB; for both materials it is difficult to collect statistics from SEM micrographs, which are at the limit of our resolution and are limited to small portions of the surface. We therefore performed nitrogen adsorption experiments (see the *Supporting Information*, Fig. SI2c) which are able to quantify the pore size distribution of the entire sample and extract information about the pore topologies. For RPB, the adsorption/desorption cycle exhibited H1 hysteresis loops, with parallel branches typical of mesoporous materials with a regular array of cylindrical pores.[34,35] On the other hand, WC8 was characterized by an H2 hysteresis loop that is typical of materials with interconnected networks of pores or ink-bottle-shaped pores.[34,35] The adsorption results confirm the visual

analysis of the pore topology based on TEM/SEM micrographs. Summarizing, the cages of WC8 form nanoroughness at their interconnections; on the contrary the porosity of RPB sample closely resembles end-capped, non-intersecting cylinders with a diameter which varies slightly along the length. The schematic representation of the pore topologies described above are illustrated in the insets of Figs. 1a and b taking into account both SEM/TEM analysis and nitrogen adsorption experiments.

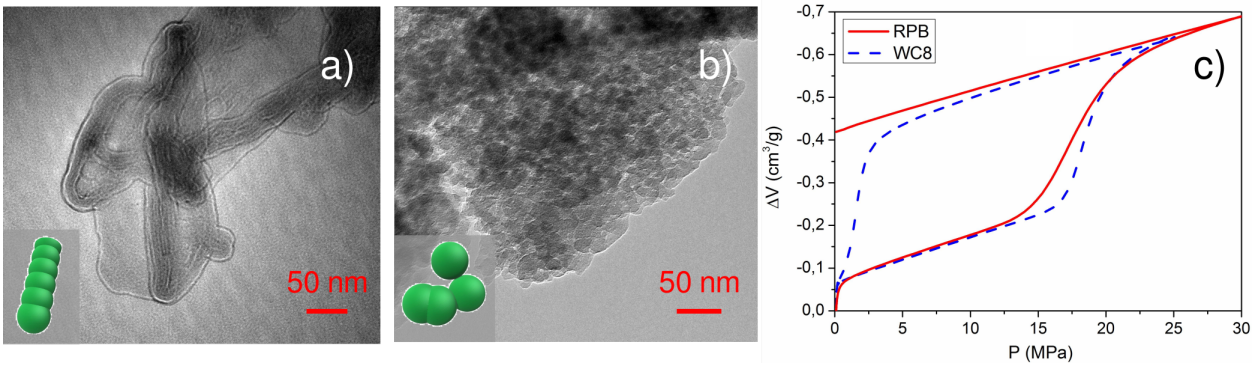

Figure 1: TEM micrographs of the RPB (a) and WC8 (b) samples, showing the semi-independent pores and the highly interconnected ones characterizing the two materials, respectively. Insets are schematic representations of the pore topology. c) Experimental intrusion and extrusion cycles for (RPB + water) and (WC8 + water). The (RPB + water) HLS did not show extrusion upon decreasing the pressure to the ambient value, while complete expulsion of water was observed for (WC8 + water) HLS.

The nominal size of the pores is similar for the two materials, with WC8 characterized by slightly larger pores than RPB as confirmed by the pore size distributions of Fig. SI2d: the typical size of the pores is 6 ± 1.5 nm for RPB and 9 ± 2.5 nm for WC8, with a small shoulder at 3.5 nm for RPB. Previous results have demonstrated the generic trend that free-energy barriers for the formation of a confined vapor phase decrease as the size of confinement is decreased;[22,25,27,36] therefore, based solely on the simplest information about the pores – their dimensions and surface chemistry – one would expect that the transition from wet pores to dry ones is favored[6,31] in the RPB case. It will be shown in the following that this simplistic prediction is not fulfilled because of the nontrivial role that pore topology plays in extrusion.

The main experiment consists in intrusion-extrusion cycles on a system comprising water as the non-wetting liquid and hydrophobized RPB and WC8 as the porous materials. The

cycles were performed by varying quasi-statically the pressure, which facilitates the comparison with the theory. The results are reported in Fig. 1c. The two samples have a similar behavior while increasing the pressure from the ambient value: for RPB intrusion occurred at ca. 17 MPa and for WC8 at ca. 18 MPa, which is compatible with the expectations for hydrophobic pores of few nanometers. On the other hand, the extrusion branch of the experiments were in stark contrast with the initial expectation, showing completely different properties when the pressure is decreased: in the case of RPB, there were no signs of extrusion, while, in the case of WC8, complete extrusion was observed in a repeatable manner at 2 MPa. In the following we try to address this surprising behavior by closely analyzing the effect of pore morphology on extrusion.

The fact that the porous matrix and the coating are the same for the two systems allows to rule out the explanation that water chemisorbs differently on the two materials. In addition, the experiments of Section *Generalizing the effect of microroughness on the extrusion pressure* show the same difference in extrusion behavior is observed when the intruding liquid is mercury, the porous materials are different, and there is no coating. Overall, the intrusion-extrusion results combined with the materials characterization (Fig. 1) suggest that subtle differences in the pore topology could be at the origin of the qualitatively different extrusion behavior of the two systems. In the next sections we present a macroscopic theory and molecular dynamics simulations targeted at elucidating the microscopic mechanism giving rise to extrusion. Given the randomness of the porous materials, we do not aim at building a realistic model of the pores but rather to understand what are the generic geometrical and/or chemical characteristics which influence the extrusion properties of a porous material. Combining macroscopic arguments and more detailed atomistic simulations allowed us to rationalize the experimental results and yields a plausible explanation for the reported extrusion behavior.

Extrusion: Theory

In order to understand the extrusion behavior of the two porous materials, it is important to remark that during extrusion the system must overcome the free-energy barrier associated with the formation of a vapor (or gas) *bubble* replacing the liquid[6,27,31] – in other words, extrusion is a nucleation process. In the case of hydrophobic cavities, it has been shown[27,30,37] that this bubble forms preferentially at specific locations of the cavity walls and that the free-energy barrier $\Delta\Omega^\dagger$ is determined by the balance of the free-energy cost of forming a liquid/vapor interface, only partly balanced by the reduction of contact area between water and the hydrophobic solid, and the free-energy gain due to the filling of the cavity by the stable vapor phase. The extrusion time depends exponentially on the barrier determined by this competition:[38]

$$t = t_0 \exp[\Delta\Omega^\dagger/(k_B T)] \ , \tag{1}$$

where the pre-exponential factor t_0 has a typical value of 10^{-12} s.[19,39] When the barrier is much higher than the thermal energy available to the system, $\Delta\Omega^\dagger \gg k_B T$, the extrusion time exceeds the typical experimental time and, in practice, no extrusion is observed.

This process is the confined analogue of vapor nucleation in bulk water;[38] for the present case, however, the surface chemistry and the geometry of the cavity become important. In order to connect the free-energy barrier to the characteristics of the cavity, we use a combined approach: 1) we employ the (computationally inexpensive) macroscopic sharp-interface model, which is described in detail below, to determine the dependence of the free-energy barrier on the morphology of the pores in terms of simple experimental parameters such as the geometry of the pore, the surface chemistry of the material, and the liquid/solid contact area and 2) we validate these results and obtain microscopic insights from molecular dynamics. We remark that, despite its simplicity, the sharp-interface model can give semi-quantitative results for cavities as small as 10 nm.[30]

The sharp-interface model assumes that the thermodynamic quantities related to the

different phases, *e.g.*, density and pressure, are constant up to the mathematical dividing interface, where there is a sharp change in these properties. For the present case of a pore partially filled with liquid, three phases are present: (fixed) solid, liquid, and vapor. According to the sharp-interface model, the free energy of such a system is:[19,37,40]

$$\Omega = \Delta P(1-\Phi)V_p + \gamma A_{lv} + \gamma_{sv}A_{sv} + \gamma_{sl}A_{sl} + \text{const} \tag{2}$$

where $\Delta P = P_l - P_v = 0$, where P_l and P_v are the pressures of the bulk liquid water and vapor, respectively, $\Phi \equiv V_l/V_p$ is the filling fraction defined by the ratio between the liquid volume V_l and the total volume of the pore V_p, A_{lv}, A_{sv}, and A_{sl} are the liquid-vapor, solid-vapor, and solid-liquid surface areas, respectively, and γ, γ_{sv}, and γ_{sl} are the corresponding surface tensions. As for any thermodynamic potential, Ω is known up to a constant, which is always set to zero in the following expressions. The first term on the RHS of Eq. (2) corresponds to the energy of the bulk liquid and vapor in a system containing both phases. The other three terms account for the energy cost/gain related to the formation of liquid-vapor, solid-liquid, and solid-vapor interfaces. Introducing Young's law $\cos\theta_Y \equiv (\gamma_{sv} - \gamma_{sl})/\gamma$, it is possible to recast Eq. (2) into the form:[21,22]

$$\Omega = \Delta P(1-\Phi)V_p + \gamma\big(A_{lv} + A_{sv}\cos\theta_Y\big) + \text{const} \tag{3}$$

which underscores the competition between γ_{sv} and γ_{sl} and provides a geometric interpretation of capillarity, distinguishing between hydrophobic surfaces (for which $\theta_Y > 90^\circ$ implies a free-energy gain from drying) and hydrophilic ($\theta_Y < 90^\circ$) ones.

The next ingredient required to compute the free-energy barriers (and thus the nucleation kinetics) is the extrusion path and the associated free-energy.[41] Here we use the Continuum Rare Event Method – CREaM[37,42,43] – in which the extrusion path consists of the sequence of the meniscus morphologies having lowest free energy at each value of the filling fraction Φ. The extrusion path originating from this prescription is a sequence of spherical-cap menisci

meeting the interior of the pore with contact angle θ_Y. In particular, the vapor bubble delimited by the meniscus increases its volume $V_v = (1-\Phi)V_p$ during extrusion, encompassing the range between the fully wet ($\Phi = 1$) and the empty state ($\Phi = 0$). Within the CREaM framework A_{lv} and A_{sv} are a function of Φ and, after setting the remaining thermodynamic parameters to the experimental values, it was possible to evaluate *via* Eq. (2) the free-energy *profile* as a function of Φ.

The CREaM approach explained above is applied to minimal pore models designed to capture the essential topology of the experimental pores together with their dimension and surface chemistry: the independent pores of RPB are schematized as smooth spherical caps of radius $r_p = 5$ nm, with a mouth of radius $r_m = 4$ nm, and with $\theta_Y = 115°$ (Fig. 2a, left). The pore model for WC8 will be presented below. Figure 2a reports the free-energy profile connected with extrusion from the smooth pore with spherical-cap geometry at $\Delta P = 0$ MPa (cyan line). These parameters have been chosen to match approximately the experimental materials and conditions. In particular, the theoretical intrusion pressure computed for our model *via* the macroscopic (sharp-interface) Laplace's law $\Delta P_{int} = -2\gamma\cos(\theta_Y + \alpha)/r_m \approx$ 23 MPa, is in fair agreement with the experimental value, with $\gamma = 0.072$ N/m and $\alpha = 15°$, where α is the re-entrant angle of the pore mouth in Fig. 2a.

The free-energy profile in Fig. 2a shows a local minimum (metastable state) in correspondence of the fully wet state at $\Phi = 1$, a maximum (unstable state, also referred to as *transition state*), and the absolute minimum (stable state) at $\Phi = 0$, with the meniscus pinned at the pore mouth corresponding to the extruded liquid (not shown). The extrusion free-energy barrier is defined as $\Delta\Omega^\dagger = \Omega_{ts} - \Omega_f$, where Ω_{ts} and Ω_f are the free energy of the *t*ransition *s*tate (free-energy maximum) and of the *f*illed pore, respectively.

In order to illustrate how changing the pressure determines extrusion, we now follow a thought experiment, assuming a slow variation of the pressure in agreement with the quasi-static experimental procedure. At the beginning of the extrusion process, when the pressure is high (30 MPa in the present experiments), the system is in the fully wet state

at $\Phi = 1$; there the free energy is lower than that at $\Phi = 0$, *i.e.*, $\Delta\Omega = \Omega_e - \Omega_f > 0$ and the *f*illed state is more stable than the *e*mpty one. As the pressure decreases, $\Delta\Omega$ becomes smaller and eventually, at sufficiently low pressures, becomes negative and the empty state is more stable than the filled one. However, the barrier $\Delta\Omega^\dagger$ might still be too large, determining the condition $t \gg t_{exp}$, where t_{exp} is the experimental time, and the extrusion is not observed. Further reducing the pressure the barrier $\Delta\Omega^\dagger$ becomes small enough ($\Delta\Omega^\dagger \approx 25 k_B T$, corresponding to $t = 1$ s) such that $t \leq t_{exp}$ and extrusion takes place. Since $\Delta\Omega^\dagger$ is an increasing function of ΔP, to understand if a transition can be observed on the experimental timescale at positive pressures it is sufficient to compute the free-energy barrier at $\Delta P = 0$. The sharp-interface model of the pores yields $\Delta\Omega^\dagger \approx 400\ k_B T$ at $\Delta P = 0$, (see Fig. 2a, cyan line) which implies a nucleation time $t \approx 10^{161}$ s, much larger than the age of the universe. Only for barriers of the order of 25 $k_B T$ is it possible to observe a transition in an experimentally relevant time.

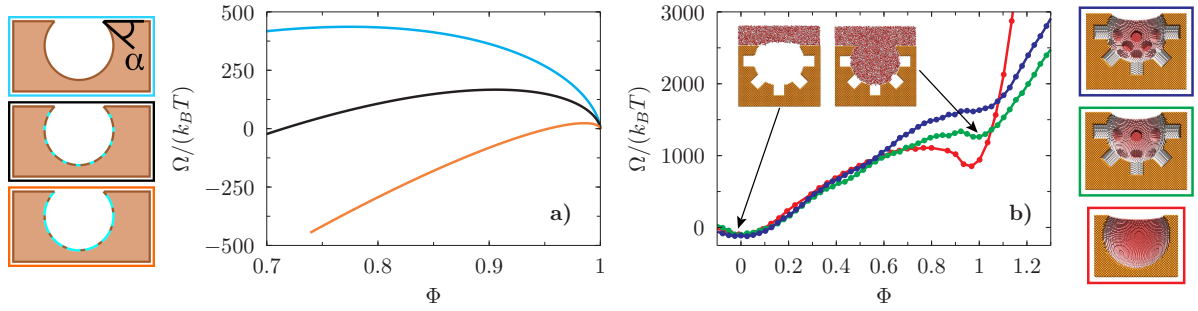

Figure 2: Free energy as a function of the filling fraction computed *via* a) the macroscopic sharp-interface model and b) *via* free-energy molecular dynamics simulations for the pore geometries reported on the side panels with the same color code. a) The free-energy profiles close to $\Phi = 1$ are calculated for $\theta_Y = 115°$ and for three values of solid fraction $\chi_s = 1$ (cyan), $\chi_s = 0.62$ (black), and $\chi_s = 0.23$ (orange) as illustrated in the sketches on the left, where light blue lines represent dry microroughness within the pore walls. b) The atomistic results are computed for $\theta_Y = 118°$ and different solid fractions: smooth ($\chi_s = 1$, red), $\chi_s = 0.65$ (green), and $\chi_s = 0.47$ (blue); the related free-energy barriers are $\Delta\Omega^\dagger = 155\, k_B T$, $45\, k_B T$, and $5\, k_B T$, respectively. The insets illustrate two different level of intrusion of the pore by water corresponding to the free-energy minima of the $\chi_s = 0.65$ case.

The previous results show that the smooth, spherical-cap pore model with contact angle and size approximately matched to the experimental ones, does not exhibit extrusion at

positive pressures. This result is in agreement with the behavior of RPB (Fig. 1a) but in marked contrast with that of WC8 (Fig. 1b): the free-energy barrier must be much lower for WC8 in order to allow for extrusion. Since this discrepancy cannot be ascribed to a difference in the surface chemistry (for water the maximum θ_Y is limited to ca. 115°), we propose that it is associated to the nanometer-sized pore interconnections present in WC8 which effectively decrease the solid-liquid contact within the pores. Indeed, owing to their small size and hydrophobicity, such small pores interconnections 1) are not intruded at the pressures at which the main pore is and 2) even if they become intruded at much higher pressures, they are likely to spontaneously dry as soon as the pressure is decreased close to $\Delta P = 0$.[6,7,29,30,32] The deeper reason why these nanoscale interconnections are always dry under ambient conditions is that the free-energy barriers decrease as the size of confinement is decreased,[22,25,36] up to the point in which the wet state is not a minimum anymore.[32] As confirmed below by molecular dynamics simulations (see Section *Extrusion: Molecular Dynamics* and Fig. SI8 of the *Supporting Information*), the main effect of pore interconnections is thus that of permanently replacing a portion of the solid-liquid contact with a liquid-vapor one (at least at $\Delta P = 0$) forming, within the pore, a composite liquid-solid-vapor interface quite distinct from smooth pores as, *e.g.*, the independent RPB pores. In other words, it is highly likely that, within pore interconnections, a nanoscale bubble is always present considerably facilitating extrusion. With this effect in mind, we further simplify our model of pore interconnections by substituting them with a rough internal surface with nanometer-sized textures (Fig. 2) remaining dry at all experimental conditions.

The effect of dry roughness can be included effectively in the free energy (3) by considering the solid area fraction $\chi_s = A_s/A_p$ where A_s is the area of the spherical cap occupied by the solid and A_p is the total area of the spherical cap. This is the fraction of internal solid surface that can actually get in contact with the liquid:

$$\Omega = \Delta P(1-\Phi)V_p + \gamma\big\{A_{lv} + A_{sv}[\chi_s(\cos\theta_Y + 1) - 1]\big\} \tag{4}$$

where A_{sv} has to be understood as the *nominal* solid-vapor area, *i.e.*, the area one would measure for the extrusion from a smooth spherical-cap pore. We remark that Eq. (4) is obtained following the classical derivation[44] for the free energy of a liquid deposited on a composite liquid-solid and solid-vapor interface. [In the superhydrophobic community the concept of apparent or Cassie-Baxter contact angle θ_{CB} is often introduced in order to describe the homogenized free-energy of a surface in the superhydrophobic state.[44–46] This angle is connected to the additional terms in Eq. (4) *via* the Cassie-Baxter law $\cos\theta_{CB} = \chi_s(\cos\theta_Y + 1) - 1$.] The free-energy profiles relative to $\chi_s = 1$ (smooth spherical-cap), $\chi = 0.62$, and $\chi_s = 0.23$ in Fig. 2a (cyan, black, and orange lines) show a progressive reduction of the free-energy barriers as the solid fraction is reduced. In particular, for $\chi_s = 0.23$, $\Delta\Omega^\dagger \approx 25\ k_BT$ and it is possible to obtain extrusion on the timescale of seconds even from a surface with a standard hydrophobic surface chemistry (*e.g.*, the maximum achievable with water is around $\theta_Y = 115°$).

The macroscopic model presented above suggests that a viable explanation of the observation of extrusion in WC8 is the presence, on the pore walls, of internal *dry* nanocavities. This scenario is compatible with the hydrophobicity of silanized silica, with the experimental intrusion pressure, and with the difference in the pore interconnections between RPB (independent pores) and WC8 (interconnected pores). In order to confirm whether this macroscopic prediction is actually verified at the scale of the experimental pores, atomistic simulations of a nanopore with internal roughness were performed and are presented in the next section.

Extrusion: Molecular Dynamics

The system considered in the molecular dynamics (MD) simulations consisted of a pore excavated from a Lennard-Jones (LJ) FCC crystal in contact with (liquid and/or vapor) TIP4P water. The basic pore geometry was a spherical cap with a radius of 5 nm and a mouth radius of ca. 4 nm (Fig. 2b), which are close to the nominal dimensions of the actual

pores (Fig. 1a-b). The solid particles interacted with the oxygen atoms of the water molecules by the modified LJ potential $v_{LJ,O}(r) = 4\epsilon\left[(\sigma/r)^{12} - c\,(\sigma/r)^{6}\right]$, where the parameter c, set to 0.85, allowed us to tune the Young contact angle to $\theta_Y = 118°$, close to the value of the actual samples, $\theta_Y = 115°$. A second set of pores with internal roughness was considered; these systems were obtained starting from smooth spherical-cap pores and excavating, from the internal surface of the sphere, a different number of cylindrical nanocavities of radius 1.25 nm and depth 2.2 nm. This procedure allowed us to obtain two different solid fractions: $\chi_s = 0.65$ and $\chi_s = 0.47$ (Fig. 2, green and blue lines, respectively). We refer to this second geometry as the *bomb* (the reason for this wording is that the geometry of these cavities is similar to the negative of a naval mine). All MD simulations were performed at constant number of particles, constant temperature, and controlling the liquid pressure *via* a piston.[47]

In order to obtain the atomistic free-energy barrier for extrusion and thus have a direct comparison with the sharp-interface calculations of Fig. 2a, we computed the atomistic free-energy profile as a function of the filling fraction for the bomb geometries with $\chi_s = 0.65$ and $\chi_s = 0.47$ and for the smooth spherical-cap pore ($\chi_s = 1$, Fig. 2b; further details on the free-energy method are included in the *Methods* section). In this "discrete" case the definition of the filling fraction is $\Phi \equiv (N - N_e)/(N_f - N_e)$, with N_e and N_f the number of particles in the pore in the empty and filled states, respectively, at $\Delta P = 0$. With this definition, it is possible to observe the conditions $\Phi > 1$, when the liquid is compressed (smooth cavity) or penetrates the smaller cavities (model pore with interconnection), and $\Phi < 0$, when the meniscus is curved towards the external part of the cavity. The extrusion free-energy barrier thus computed was $\Delta\Omega^{\dagger} = 155\ k_BT$ for the smooth pore at $\Delta P = 0$ MPa (Fig. 2): this high barrier kinetically prevents liquid extrusion at positive pressures. Comparison of the free-energy profiles for the smooth and bomb cases in Fig. 2b underscores that the presence of nanocavities significantly reduced the extrusion barrier, as expected from the macroscopic model. In particular, for $\chi_s = 0.47$, $\Delta\Omega^{\dagger}$ is lower than $25\,k_BT$, which implies that this geometry is a good candidate to observe extrusion during an experiment of few

seconds. It is worth mentioning that the value predicted by the sharp-interface model to obtain a transition was $\chi_s = 0.25$, which is a rather conservative estimate as compared to this atomistic prediction. This difference is connected to the fact that the free-energy barriers computed in the sharp-interface approximation are typically larger[48] than those predicted by atomistic simulations due to the presence of diffuse interfaces.

Finally, we remark that, consistently with the hypothesis put forward in the previous section, at $\Delta P = 0$ cylindrical nanocavities are always devoid of liquid, as one deduces from the absence of any minimum of the free energy in correspondence to the their wet state ($\Phi > 1$).

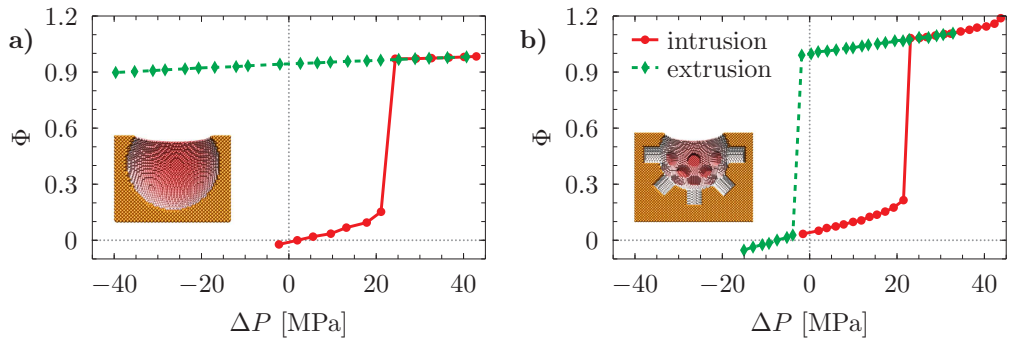

Figure 3: a) Filling of the pore as a function of the applied pressure during an in silico experiment in which the pressure was increased (red) and subsequently decreased (green). b) Pore filling as a function of pressure for an in silico intrusion (red) and extrusion (green) experiment on a spherical-cap pore with internal roughness with $\chi_s = 0.47$. Unlike in the case of the smooth pore in a), the pore is completely emptied at slightly negative pressures.

The (computationally expensive) free-energy simulations, performed at $\Delta P = 0$, suggested that internal roughness or pore interconnections indeed facilitate extrusion. In order to ensure that this behavior is actually observed in experiments in which the pressure is varied, we performed the *in silico* equivalent of the experiments in Fig. 1c, see also Ref.[49] Figure 3 reports the simulated intrusion and extrusion cycle for the smooth pore and for the bomb with $\chi_s = 0.47$ at $T = 300$ K. The simulation details are found in the *Methods* section and in the *Supporting Information*.

The numerical experiment for the smooth pore (Fig. 3a) was initialized with the pore

in the empty state ($\Phi = 0$) at $\Delta P = 0$ MPa. As the pressure was increased, the pore remained empty with the meniscus pinned at the mouth and progressively sagging into the pore ($\Delta P < 23$ MPa). When a critical pressure value (*intrusion pressure*) was reached, $\Delta P_{int} = 23$ MPa, water abruptly wet the pore, reaching $\Phi = 1$. The value of the MD intrusion pressure was close to the experimental one and in fair agreement with the macroscopic expectation given by Laplace's law, $\Delta P_{int} \approx 21$ MPa, where the values $\gamma = 0.062$ N/m (the surface tension of TIP4P-Ew water[50]), $\alpha = 15°$, $\theta_Y = 118°$, and $r_m \approx 4$ nm were used. Finally, any further increase of the pressure produced minor changes in Φ due to the low compressibility of water.

From the condition $\Delta P = 50$ MPa and $\Phi = 1$, the pressure was progressively decreased (green line in Fig. 3a). At the minimum pressure reached in the actual experiments, $\Delta P = 0$, we did not observe extrusion of water out of the pore: this behavior is compatible with RPB, for which no extrusion was observed (Fig. 1c). Unlike in experiments, in the MD intrusion/extrusion cycle the time amenable of simulations is few nanoseconds; therefore, we had to continue depressurizing the system down to negative pressures (tensile state) in order to facilitate extrusion[6,49] – in other words, in MD extrusion can only be observed when $\Delta\Omega^{\dagger}$ is smaller than in experiments. Even at large negative pressures ($\Delta P \approx -40$ MPa, when the liquid is under tension) water completely wets the pore without extrusion. These extreme tensile conditions are difficult to explore in experiments but are easily accessible to simulation.

The same protocol was followed for the bomb geometry (Fig. 3b): the intrusion part of the process was equivalent to the smooth pore, with the transition from the empty to the fully wet state triggered at $\Delta P_{int} = 23$ MPa. Instead, during decompression, when the system reached a pressure $\Delta P_{ext} = -2$ MPa, a bubble nucleated within the pore and the liquid extruded from the pore restoring the empty state (the reason for the relatively small negative extrusion pressure is explained in the following). The comparison of the two virtual intrusion-extrusion experiments in Fig. 3 clearly show that surface roughness

within the pores plays an important role in determining the behavior of a porous material, causing a radically different extrusion behavior, even when the intrusion behavior is similar. Finally, contrasting Fig. 1c and Fig. 3 demonstrates that our atomistic models capture the behavior of RPM and WC8 pores under intrusion-extrusion experiments, based on minimal ingredients: they have roughly the same sizes, identical surface chemistry ($\theta_Y = 118°$) but different topologies that allows for extrusion in the case of the interconnected WC8 pores (Fig. 1).

In Fig. SI7 of the *Supporting Information* we analyze the effect of internal roughness on the cycle when the maximum pressure is significantly larger than the intrusion one for the main pore. In this case, the presence of internal roughness causes a small additional intrusion/extrusion loop due to the wetting of these nanocavities at very large pressures. This second loop, however, becomes undetectable in actual experiments if the internal roughness has a volume much smaller than the main pores, as expected for pore interconnections.

At a variance with the actual experiment, in the MD pressure cycle a relatively small negative extrusion pressure was recorded (we remind that no extrusion was observed in the smooth case). As explained above, the exact value of the extrusion pressure depends on the timescale of the experiment as implied by the expression for $t(\Delta P)$, with longer timescales corresponding to higher pressures, see, *e.g.*, Fig. 5a of Ref.[6] In the MD experiment the timescale was of the order of 10^{-9} s while in the actual experiment it was ca. 1 s. This difference in the timescales therefore can explain the quantitative discrepancy between the MD and the experimental extrusion pressures, which is due to the much shorter timescale accessible to MD. The quantitative discussion of this point is beyond the scope of this paper and will be investigated in a forthcoming work.

Altogether, the simulation campaign has shown that the characteristics of the internal surface of a porous material critically affect its extrusion behavior. In particular, a second tier of smaller nanocavities in the internal surface of the main pores, corresponding to surface roughness or to the interconnections between pores, facilitates the drying of the pores – a

result which accounts for the reported experimental behavior. Such findings shed light on how the fine features of a porous material influence pressure hysteresis – a step which enables the control and optimization of the energy-related capabilities of such materials.

In addition to porous materials for energy applications, the present results are also relevant for understanding the wetting and drying of superhydrophobic surfaces with different scales of roughness: in this context, empty and wet states of the pores correspond to the Cassie-Baxter[44] (superhydrophobic) and Wenzel[51] (non superhydrophobic) states of the nanotexture, respectively. The present results demonstrate that a surface with hierarchical textures, *e.g.*, with the smaller roughness on the 1 nm scale and a larger one, facilitates the recovery of the superhydrophobic state on the large scale *without* the need of an external energy supply: the smaller nanocavities reduce the solid-liquid contact facilitating the expulsion of the liquid from the larger pore. A clear paradigm emerges for engineering the recovery of the superhydrophobic state, *i.e.*, the use of hierarchical textured surface. Such principle was proposed in a previous theoretical work[32] and its effectiveness is substantiated by the present molecular dynamics simulations.

Generalizing the effect of microroughness on the extrusion pressure

In order to demonstrate the generality of these conclusions, two additional HLSs based on mercury and different porous silica were subject to intrusion-extrusion experiments. Mercury was chosen as the most common non-wetting liquid with well-developed experimental protocols. The fact that mercury forms large contact angles ($\theta_Y \approx 140°$, satisfying the non-wetting condition $\theta_Y > 90°$) with nearly all the common materials, allows to use porous materials *without grafting* for intrusion-extrusion cycling experiments. This characteristic significantly broadens the range of available nanoporous materials, giving access to model-like topologies. In particular, MCM-41 porous silica was used, which presents model-like non-intersecting uniform cylindrical pores (Fig. 4b). Another porous silica, G60, represents disordered pores with intersections of different sizes including micropores (Fig. 4d).

By comparing Figs. 4a and c, a drastic difference in intrusion-extrusion pressure hysteresis is apparent: for (MCM-41 + mercury) the difference between intrusion and extrusion pressures is very large – more than 200 MPa. For (G60 + mercury), instead, intrusion-extrusion hysteresis is negligible, even though the pores of G60 silica are, on average, about 2 nm larger than those of MCM-41. Such difference becomes particularly apparent in a differential representation, when one compares the peaks of compressibility ($\mathrm{d}V/\mathrm{d}P$) for the intrusion and extrusion steps (Fig. 4a and c). We attribute the negligible pressure hysteresis of (G60 + mercury) to the microroughness present in G60 silica – the intersections of the disordered pores. Such microroughness is visible in the TEM micrographs (Fig. 4d) and is reflected in the compressibility curve presenting a secondary peak corresponding to pores with characteristic size less than 4 nm (Fig. 4c). Such roughness seems to facilitate the extrusion process as in the bomb geometry and, as a result, the extrusion from (8.0 - 5.5) nm pores is non-hysteretic (Fig. 4c). On the contrary, MCM-41 does not present any microroughness in addition to the highly-ordered, non-intersecting pores in the (4.5 - 3.5) nm range (Fig. 4b); this structure results in a highly hysteretic intrusion-extrusion cycle (Fig. 4a). The present results for mercury are consistent with those of Ref.,[52] where mercury porosimetry data were shown to have lower intrusion-extrusion hysteresis when the pores had higher surface fractal dimension.

The significant difference in the pressures hysteresis reported for (MCM-41 + mercury) and (G60 + mercury) is in agreement with the conclusions of the previous sections on water and demonstrate that hysteresis in intrusion-extrusion cycles can be controlled solely by means of pore topology for a variety of non-wetting liquids. This understanding may be used to design the optimal topology of the pores to achieve the desired functional properties, *e.g.*, an intrusion-extrusion cycle with controlled hysteresis.

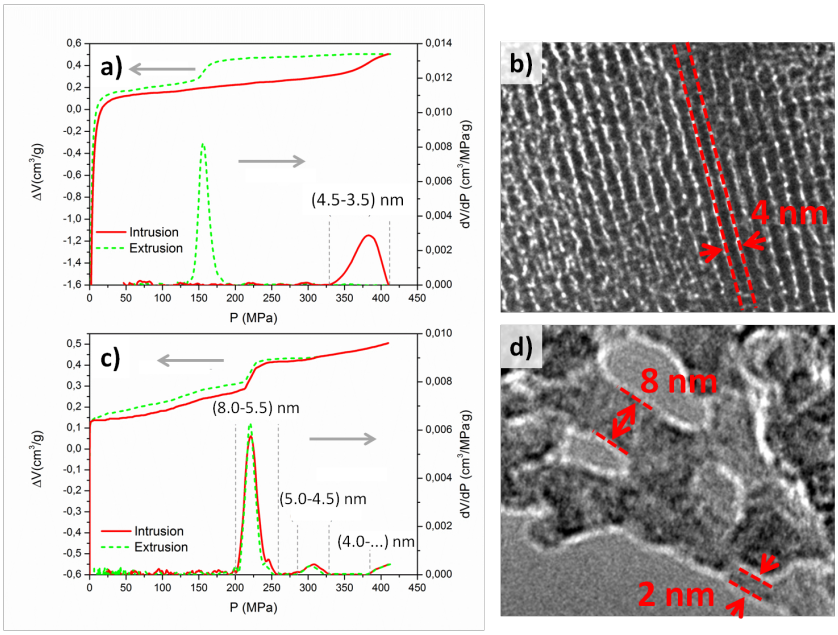

Figure 4: Experimental intrusion and extrusion cycle and compressibility for a) (MCM-41 + mercury) and c) (G60 + mercury) HLSs. TEM-micrographs of b) MCM-41 and d) G60 silica. The pore sizes indicated in the compressibility graphs a) and c) are obtained from mercury porosimetry technique by relating intrusion pressure with the pore radius through Laplace's law.

Conclusions

In this paper, the effect of the internal topology of porous materials on the extrusion of non-wetting liquids has been investigated *via* experiments and molecular dynamics simulations. Concerning experiments, isothermal pressure cycles were performed on two samples with similar nominal pore characteristics but qualitatively different extrusion behaviors: surprisingly, the material characterized by larger pores extruded (WC8) when depressurized while the other did not (RPB). Nitrogen adsorption experiments and TEM micrographs of the two samples confirmed that the pore sizes were comparable but the pore topology was different: WC8 has highly interconnected pores, while RPB semi-independent ones. In order to understand the effect of these fine characteristics of the pores on the extrusion behavior a minimal theoretical model of the pore was employed. A macroscopic, sharp-interface model for liquid extrusion shed light on two aspects: i) it explained in terms of free-energy barriers the lack of extrusion and ii) it allowed us to understand what is a crucial characteristic to

achieve extrusion, *i.e.*, a secondary scale of roughness at the inner surface of the pores, *e.g.*, due to intricate pore interconnections. The presence of such roughness gives rise to a *superhydrophobic* state at the pore walls and reduces liquid/solid contact area, facilitating the creation of the extrusion bubble. A lower solid fraction corresponds to a lower nucleation free-energy barrier which, in turn, controls the time needed to observe a transition from the fully wet to the dry state, *i.e.*, extrusion.

This macroscopic prediction was corroborated by molecular dynamics simulations of intrusion and extrusion in a spherical-cap pore with smaller cylindrical nanocavities on its surface, which indeed showed water extrusion upon depressurization as opposed to a spherical-cap pore *without* such nanocavities. Atomistic free-energy calculations further showed that 1) the nanometer-sized roughness remains empty at the experimental pressures and 2) extrusion is observed at a value of solid fraction larger than the (conservative) macroscopic predictions.

These findings were further generalized by performing mercury intrusion-extrusion experiments for two porous silica with significantly different topologies: MCM-41 - highly-ordered non-intersecting cylinders and G60 - disordered pores with microroughness due to the numerous intersections. A drastic difference in mercury intrusion-extrusion pressure hysteresis for these two materials was observed, with G60 showing almost no hysteresis. This result confirmed the paramount importance of microroughness and pore interconnections in favoring liquid extrusion independently of the specific non-wetting liquid employed.

Summarizing, experiments combined with macroscopic and atomistic models suggest that the qualitatively different extrusion behaviors observed for mesoporous materials depend on the characteristics of the inner surface of the pores, in particular, on the number of pore interconnections. This material parameter can be used to tailor the extrusion behavior of porous materials. In addition to experimental evidence, the presented theories constitute a comprehensive framework to predict the intrusion and extrusion behavior of porous materials based on their topology. These results may prove instrumental to advance a wide range of

applications rooted in nanoscale capillary phenomena including superhydrophobic surfaces, nanofluidics, energy storage, drug delivery, oil-water separation, and oil extraction.

Methods

Experimental materials and methods

Materials: In this work we used two HLSs based on distilled water: (RPB + water) and (WC8 + water). WC8 is a commercial mesoporous silica gel in the shape of 6-8 μm granules grafted with the octylsilanes C8 with a density of 2.1 groups/nm^2 according to the data provided by the supplier (SymmetryPrep C8 by Waters). WC8 stands for Waters C8. RPB is another commercial mesoporous silica gel grafted in the same way as WC8 (LiChroprep RP-select B by Merck). Additionally, we used two HLSs based on mercury: (G60 + mercury) and (MCM-41 + mercury). G60 is a commercial mesoporous silica from Davisil, where G60 stands for Grace 60Å. MCM-41 porous silica was synthesized following the protocol[53] described below. Tetraethylorthosilicate (TEOS) and cetyltrimethylammonium bromide (CTAB) were used as the source of silicon and structure directing agent, respectively. CTAB (1.4 g) was added to deionized water (60 mL) in a 150 mL beaker while the mixture was stirred at room temperature. After 10 min, ammonium hydroxide (3.52 g) was added to the above solution under stirring for 30 min until a clear solution was obtained. Then, TEOS (3.73 g) was added drop-wise to the solution. The mixture kept stirring with 350 r.p.m speed. After 2h a milky solution was obtained; this solution was transferred into a Teflon-lined autoclave and treated under autogenous pressure without stirring at 373 K for 15 hours. Then, the solid product was filtered from the mother liquor and washed with deionized water. The sample was dried at 100 °C for 4 h. The obtained white powder was calcined at 550 °C for 5 h to remove any remaining surfactant. All chemicals and reagents used for the synthesis were purchased from Sigma-Aldrich and used without further purification.

Methods: High-pressure compression-decompression experiments were performed using Pore Master 60 mercury porosimeter from Quantachrome Instruments. For mercury based HLSs, the intrusion-extrusion experiments were executed following the standard procedure of mercury porosimetry. Namely, materials were subjected to outgassing up to 30 Pa prior to mixing with mercury. Next the system was compressed-decompressed in the required pressure range for at least 10 times to ensure repeatability. The pore size distribution was calculated using Laplace's law, using standard values of $\theta_Y = 140°$ for contact angle and $\gamma = 480$ mN/m for the surface tension of mercury. For water-based HLSs, RPB or WC8 were mixed with water and encapsulated into flexible hermetic Teflon capsules prior to the procedure described above.

Textural properties were characterized in an automated gas adsorption analyzer (Micromeritics ASAP 2460). Nitrogen sorption curves of the samples were measured, under isothermal conditions, after outgassing at 200 °C in vacuum for 5 h. The multipoint surface area was evaluated with the Brunauer-Emmett-Teller (BET) method over the range $P/P_0 = 0.075$-0.35 and pore size distribution was obtained using Barrett-Joyner-Halenda (BJH) model applied to the desorption isotherm branch. Total pore volume was determined from the volume adsorbed at $P/P_0 = 0.98$.

Transmission electron microscopy (TEM) measurements were realized by using a FEI Tecnai F20 electron microscope operating at 200 kV. For TEM measurements, samples were dispersed in ethanol and sonicated; subsequently, the resulting solution was transferred onto a holey carbon film fixed on a 3 mm copper grid (200 mesh). Additionally samples were imaged by Quanta 200 FEG scanning electron microscopy microscope operated in high vacuum mode at 30 kV featured with a Everhart-Thornley secondary electron detector.

Molecular dynamics simulations

Model: Water molecules were represented by the TIP4P-Ew model.[54] The interaction between the oxygen and the solid particles of the walls was described by the modified Lennard-

Jones (LJ) potential: $v(r) = 4\epsilon\left[(\sigma/r)^{12} - c(\sigma/r)^{6}\right]$ where r is the distance between the oxygen and the wall particles, $\epsilon = 0.16275$ Kcal/mol and $\sigma = 3.16435$ nm are the characteristic energy and length of the LJ interaction, respectively. The parameter c was tuned as to achieve the desired θ_Y, computed as the contact angle of a sessile water drop deposited on a flat substrate.[6,30] Here, we set $c = 0.85$ which corresponds to $\theta_Y = 118°$. Hydrogen and wall atoms did not interact. Periodic boundary conditions were applied in the directions parallel to the wall. The atoms of the textured surface were kept fixed during the simulation while the atoms of the upper solid surface (piston) were allowed to move only in the wall-normal direction. The system was kept at $T = 300$ K by a Nosé-Hoover-chains thermostat.[55] The molecular dynamics engine was LAMMPS.[56]

Intrusion and extrusion experiment: The MD intrusion and extrusion experiment consisted in applying a constant pressure to the system and to measure the quantity of water molecules inside the pore; after a sufficiently long simulation, the pressure was increased in steps until intrusion was achieved; eventually, the pressure was decreased to mimic the extrusion phase. The pressure of the system was controlled *via* the upper solid wall which acts as a piston on the bulk of the water outside the spherical-cap pore. A constant force f was applied to each wall atom in the direction normal to the upper wall such that, at equilibrium, the pressure of the liquid water balanced the external pressure:[47,48] $A_p P_l = f N_p$, where A_p and N_p are the area and number of particles of the piston, respectively, and P_l is the water pressure (see also the *Supporting Information*, Fig. SI5 and SI6). Finally, due to the low vapor tension P_v of water, the quantity $\Delta P = P_l - P_v$ was approximated as $\Delta P \approx P_l$. In order to compute the filling fraction Φ we defined the observable $\Xi(\boldsymbol{r})$ counting the number of water molecules in a region containing the pore. The time average $\langle \Xi \rangle$ of this observable at a given pressure was used for computing the filling fraction in Figs. 2 and 3: $\Phi = (\langle \Xi \rangle - N_e)/(N_f - N_e)$ where N_f and N_e are the number of water molecules in the fully wet and empty states, respectively. From this definition, $\Phi = 1$ and $\Phi = 0$ correspond to

the fully wet and empty states, respectively.

Free-energy computations: Experimental results and MD simulations were interpreted in terms of quasi-static theories of thermally activated events.[41,57,58] Even though these theories neglect some dynamical effects, which can be taken into account in other approaches,[59–61] they make the interpretation of results simple and intuitive.

Free-energy profiles were computed using restrained molecular dynamics (RMD), which is a static version of temperature accelerated MD.[62] In RMD the central quantity to compute is the derivative of the free-energy $d\Omega/d\Phi$ from which Ω is determined by numerical integration. RMD amounts to add a restraining potential $v_r = k/2(\Phi(r) - \Phi^*)^2$ to the physical one where $\Phi(r)$ is the filling fraction defined above. This potential, for suitably large values of the constant k, restrains the system close to the condition $\Phi(r) = \Phi^*$. In RMD, the quantity $d\Omega/d\Phi$ is given by: $d\Omega/d\Phi = k\langle(\Phi^* - \Phi(r))\rangle_{RMD}$, where the symbol $\langle\cdot\rangle_{RMD}$ denotes the time average in the RMD simulation. In a nutshell, one runs many independent RMD simulations at different values of Φ^* in order to compute $d\Omega/d\Phi$; the free-energy profile is then reconstructed by numerical integration.

Conflicts of interest

There are no conflicts to declare.

Acknowledgement

The help of Eider Mendiburu and Cristina Peña with the contact angle measurements is highly appreciated. The research leading to these results has received funding from the European Research Council under the European Union's Seventh Framework Programme (FP7/2007-2013)/ERC Grant agreement n. [339446]. SM acknowledges Sapienza University of Rome for financial support through grant RG11715C81D4F43C.

We acknowledge PRACE for awarding us access to Marconi at CINECA, Italy. This work has been supported by a grant from the Swiss National Supercomputing Centre (CSCS) under project ID s730.

Supporting Information Available

The Supporting Information is available free of charge on the ACS Publications website at DOI: 10.1021/????

Experimental details; Details on the molecular dynamics simulations.

References

1. Eroshenko, V. Effect of Heat Exchange on Filling of Lyophobic Pores and Capillaries with Liquid. *Colloid J. USSR (Engl. Transl.)* **1988**, *49*, 769–773.

2. Fadeev, A. Y.; Eroshenko, V. A. Study of Penetration of Water into Hydrophobized Porous Silicas. *J. Colloid Interface Sci.* **1997**, *187*, 275–282.

3. Eroshenko, V.; Regis, R.-C.; Soulard, M.; Patarin, J. Energetics: a New Field of Applications for Hydrophobic Zeolites. *J. Am. Chem. Soc.* **2001**, *123*, 8129–8130.

4. Grosu, Y.; Ievtushenko, O.; Eroshenko, V.; Nedelec, J.-M.; Grolier, J. Water Intrusion/Extrusion in Hydrophobized Mesoporous Silica Gel in a Wide Temperature Range: Capillarity, Bubble Nucleation and Line Tension Effects. *Colloids Surf., A* **2014**, *441*, 549–555.

5. Fraux, G.; Coudert, F.-X.; Boutin, A.; Fuchs, A. H. Forced Intrusion of Water and Aqueous Solutions in Microporous Materials: from Fundamental Thermodynamics to Energy Storage Devices. *Chem. Soc. Rev.* **2017**, *46*, 7421–7437.

6. Tinti, A.; Giacomello, A.; Grosu, Y.; Casciola, C. M. Intrusion and Extrusion of Water in Hydrophobic Nanopores. *Proc. Natl. Acad. Sci. USA* **2017**, *114*, E10266–E10273.

7. Guillemot, L.; Biben, T.; Galarneau, A.; Vigier, G.; Charlaix, É. Activated Drying in Hydrophobic Nanopores and the Line Tension of Water. *Proc. Natl. Acad. Sci. USA* **2012**, *109*, 19557–19562.

8. Eroshenko, V. Virtually Oil-Free Shock Absorber Having High Dissipative Capacity. 2015; US Patent 8,925,697.

9. Grosu, Y.; Li, M.; Peng, Y.-L.; Luo, D.; Li, D.; Faik, A.; Nedelec, J.-M.; Grolier, J.-P. A Highly Stable Nonhysteretic {Cu2 (tebpz) MOF+ water} Molecular Spring. *ChemPhysChem* **2016**, *17*, 3359–3364.

10. Iwatsubo, T.; Suciu, C. V.; Ikenagao, M.; Yaguchio, K. Dynamic Characteristics of a New Damping Element Based on Surface Extension Principle in Nanopore. *J. Sound Vib.* **2007**, *308*, 579–590.

11. Eroshenko, V.; Piatiletov, I.; Coiffard, L.; Stoudenets, V. A New Paradigm of Mechanical Energy Dissipation. Part 2: Experimental Investigation and Effectiveness of a Novel Car Damper. *Proc. Inst. Mech. Eng., Part D* **2007**, *221*, 301–312.

12. Ryzhikov, A.; Daou, T. J.; Nouali, H.; Patarin, J.; Ouwehand, J.; Clerick, S.; De Canck, E.; Van Der Voort, P.; Martens, J. A. Periodic Mesoporous Organosilicas as Porous Matrix for Heterogeneous Lyophobic Systems. *Microporous Mesoporous Mater.* **2018**, *260*, 166–171.

13. Qiao, Y.; Punyamurtula, V. K.; Han, A.; Kong, X.; Surani, F. B. Temperature Dependence of Working Pressure of a Nanoporous Liquid Spring. *Appl. Phys. Lett.* **2006**, *89*, 251905.

14. Tzanis, L.; Trzpit, M.; Soulard, M.; Patarin, J. Energetic Performances of Channel and Cage-Type Zeosils. *J. Phys. Chem. C* **2012**, *116*, 20389–20395.

15. Suciu, C. V.; Tobiishi, T. Comfortableness Evaluation of an Autovehicle Equipped with Colloidal Suspensions. *J. Sys. Design Dynam.* **2012**, *6*, 555–567.

16. Guillemot, L.; Galarneau, A.; Vigier, G.; Abensur, T.; Charlaix, É. New Device to Measure Dynamic Intrusion/Extrusion Cycles of Lyophobic Heterogeneous Systems. *Rev. Sci. Instrum.* **2012**, *83*, 105105.

17. Suciu, C. V.; Tani, S.; Miyoshi, K. Experimental Study on the Thermal Characteristics of a Colloidal Damper. *J. Sys. Design Dynam.* **2010**, *4*, 899–913.

18. Tuller, M.; Or, D.; Dudley, L. M. Adsorption and Capillary Condensation in Porous Media: Liquid Retention and Interfacial Configurations in Angular Pores. *Water Resour. Res.* **1999**, *35*, 1949–1964.

19. Lum, K.; Luzar, A. Pathway to Surface-Induced Phase Transition of a Confined Fluid. *Phys. Rev. E* **1997**, *56*, R6283.

20. Leung, K.; Luzar, A.; Bratko, D. Dynamics of Capillary Drying in Water. *Phys. Rev. Lett.* **2003**, *90*, 065502.

21. Huang, X.; Margulis, C. J.; Berne, B. J. Dewetting-Induced Collapse of Hydrophobic Particles. *Proc. Natl. Acad. Sci. USA* **2003**, *100*, 11953–11958.

22. Luzar, A. Activation Barrier Scaling for the Spontaneous Evaporation of Confined Water. *J. Phys. Chem. B* **2004**, *108*, 19859–19866.

23. Berne, B. J.; Weeks, J. D.; Zhou, R. Dewetting and Hydrophobic Interaction in Physical and Biological Systems. *Annu. Rev. Phys. Chem.* **2009**, *60*, 85–103.

24. Sharma, S.; Debenedetti, P. G. Evaporation Rate of Water in Hydrophobic Confinement. *Proc. Natl. Acad. Sci. USA* **2012**, *109*, 4365–4370.

25. Sharma, S.; Debenedetti, P. G. Free Energy Barriers to Evaporation of Water in Hydrophobic Confinement. *J. Phys. Chem. B* **2012**, *116*, 13282–13289.

26. Giacomello, A.; Meloni, S.; Chinappi, M.; Casciola, C. M. Cassie–Baxter and Wenzel States on a Nanostructured Surface: Phase Diagram, Metastabilities, and Transition Mechanism by Atomistic Free Energy Calculations. *Langmuir* **2012**, *28*, 10764–10772.

27. Giacomello, A.; Chinappi, M.; Meloni, S.; Casciola, C. M. Geometry as a Catalyst: How Vapor Cavities Nucleate from Defects. *Langmuir* **2013**, *29*, 14873–14884.

28. Vanzo, D.; Bratko, D.; Luzar, A. Dynamic Control of Nanopore Wetting in Water and Saline Solutions under an Electric Field. *J. Phys. Chem. B* **2015**, *119*, 8890–8899.

29. Prakash, S.; Xi, E.; Patel, A. J. Spontaneous Recovery of Superhydrophobicity on Nanotextured Surfaces. *Proc. Natl. Acad. Sci. USA* **2016**, *113*, 5508–5513.

30. Lisi, E.; Amabili, M.; Meloni, S.; Giacomello, A.; Casciola, C. M. Self-Recovery Superhydrophobic Surfaces: Modular Design. *ACS Nano* **2018**, *12*, 359–367.

31. Lefevre, B.; Saugey, A.; Barrat, J.-L.; Bocquet, L.; Charlaix, E.; Gobin, P.-F.; Vigier, G. Intrusion and Extrusion of Water in Hydrophobic Mesopores. *J. Chem. Phys.* **2004**, *120*, 4927–4938.

32. Giacomello, A.; Schimmele, L.; Dietrich, S.; Tasinkevych, M. Perpetual Superhydrophobicity. *Soft Matter* **2016**, *12*, 8927–8934.

33. Smirnov, S.; Vlassiouk, I.; Takmakov, P.; Rios, F. Water Confinement in Hydrophobic Nanopores. Pressure-Induced Wetting and Drying. *ACS Nano* **2010**, *4*, 5069–5075.

34. Thommes, M. Physical Adsorption Characterization of Nanoporous Materials. *Chem. Ing. Tech.* **2010**, *82*, 1059–1073.

35. Nguyen, P. T.; Fan, C.; Do, D.; Nicholson, D. On the Cavitation-like Pore Blocking in Ink-Bottle Pore: Evolution of Hysteresis Loop with Neck Size. *J. Phys. Chem. C* **2013**, *117*, 5475–5484.

36. Remsing, R. C.; Xi, E.; Vembanur, S.; Sharma, S.; Debenedetti, P. G.; Garde, S.; Patel, A. J. Pathways to Dewetting in Hydrophobic Confinement. *Proc. Natl. Acad. Sci. USA* **2015**, *112*, 8181–8186.

37. Giacomello, A.; Chinappi, M.; Meloni, S.; Casciola, C. M. Metastable Wetting on Superhydrophobic Surfaces: Continuum and Atomistic Views of the Cassie-BaxterWenzel Transition. *Phys. Rev. Lett.* **2012**, *109*, 226102.

38. Debenedetti, P. G. *Metastable Liquids: Concepts and Principles*; Princeton University Press, 1996.

39. Menzl, G.; Gonzalez, M. A.; Geiger, P.; Caupin, F.; Abascal, J. L.; Valeriani, C.; Dellago, C. Molecular Mechanism for Cavitation in Water Under Tension. *Proc. Natl. Acad. Sci. USA* **2016**, *113*, 13582–13587.

40. Evans, R.; Marconi, U. M. B.; Tarazona, P. Fluids in Narrow Pores: Adsorption, Capillary Condensation, and Critical Points. *J. Chem. Phys.* **1986**, *84*, 2376–2399.

41. Bonella, S.; Meloni, S.; Ciccotti, G. Theory and Methods for Rare Events. *Eur. Phys. J. B* **2012**, *85*, 1–19.

42. Giacomello, A.; Meloni, S.; Müller, M.; Casciola, C. M. Mechanism of the Cassie-Wenzel Transition *via* the Atomistic and Continuum String Methods. *J. Chem. Phys.* **2015**, *142*, 104701.

43. Meloni, S.; Giacomello, A.; Casciola, C. M. Focus Article: Theoretical Aspects of Vapor/Gas Nucleation at Structured Surfaces. *J. Chem. Phys.* **2016**, *145*, 211802–18.

44. Cassie, A.; Baxter, S. Wettability of Porous Surfaces. *Trans. Faraday Soc.* **1944**, *40*, 546–551.

45. Patankar, N. A. Transition between Superhydrophobic States on Rough Surfaces. *Langmuir* **2004**, *20*, 7097–7102.

46. Patankar, N. A. Consolidation of Hydrophobic Transition Criteria by Using an Approximate Energy Minimization Approach. *Langmuir* **2010**, *26*, 8941–8945.

47. Marchio, S.; Meloni, S.; Giacomello, A.; Valeriani, C.; Casciola, C. Pressure Control in Interfacial Systems: Atomistic Simulations of Vapor Nucleation. *J. Chem. Phys.* **2018**, *148*, 064706.

48. Amabili, M.; Lisi, E.; Giacomello, A.; Casciola, C. M. Wetting and Cavitation Pathways on Nanodecorated Surfaces. *Soft Matter* **2016**, *12*, 3046–3055.

49. Amabili, M.; Giacomello, A.; Meloni, S.; Casciola, C. Intrusion and Extrusion of a Liquid on Nanostructured Surfaces. *J. Phys: Condens. Mat.* **2016**, *29*, 014003.

50. Vega, C.; De Miguel, E. Surface Tension of the Most Popular Models of Water by Using the Test-Area Simulation Method. *J. Chem. Phys.* **2007**, *126*, 154707.

51. Wenzel, R. N. Resistance of Solid Surfaces to Wetting by Water. *Ind. Eng. Chem.* **1936**, *28*, 988–994.

52. Rigby, S. P.; Chigada, P. I. MF-DFT and Experimental Investigations of the Origins of Hysteresis in Mercury Porosimetry of Silica Materials. *Langmuir* **2009**, *26*, 241–248.

53. Sayari, A.; Liu, P.; Kruk, M.; Jaroniec, M. Characterization of Large-Pore MCM-41 Molecular Sieves Obtained *via* Hydrothermal Restructuring. *Chem. Mater.* **1997**, *9*, 2499–2506.

54. Horn, H. W.; Swope, W. C.; Pitera, J. W.; Madura, J. D.; Dick, T. J.; Hura, G. L.; Head-Gordon, T. Development of an Improved four-site Water Model for Biomolecular Simulations: TIP4P-Ew. *J. Chem. Phys.* **2004**, *120*, 9665–9678.

55. Martyna, G. J.; Klein, M. L.; Tuckerman, M. Nosé–Hoover Chains: the Canonical Ensemble *via* Continuous Dynamics. *J. Chem. Phys.* **1992**, *97*, 2635–2643.

56. Plimpton, S. Fast Parallel Algorithms for Short-Range Molecular Dynamics. *J. Comp. Phys.* **1995**, *117*, 1–19.

57. Zwanzig, R. *Nonequilibrium Statistical Mechanics*; Oxford University Press, 2001.

58. Vanden-Eijnden, E. *Computer Simulations in Condensed Matter Systems: From Materials to Chemical Biology Volume 1*; Springer, 2006; pp 453–493.

59. Allen, R. J.; Valeriani, C.; ten Wolde, P. R. Forward Flux Sampling for Rare Event Simulations. *J. Phys: Condens. Mat.* **2009**, *21*, 463102.

60. Orlandini, S.; Meloni, S.; Ciccotti, G. Hydrodynamics from Statistical Mechanics: Combined Dynamical-NEMD and Conditional Sampling to Relax an Interface between two Immiscible Liquids. *Phys. Chem. Chem. Phys.* **2011**, *13*, 13177–13181.

61. Pourali, M.; Meloni, S.; Magaletti, F.; Maghari, A.; Casciola, C. M.; Ciccotti, G. Relaxation of a Steep Density Gradient in a Simple Fluid: Comparison between Atomistic and Continuum Modeling. *J. Chem. Phys.* **2014**, *141*, 154107.

62. Maragliano, L.; Vanden-Eijnden, E. A Temperature Accelerated Method for Sampling Free Energy and Determining Reaction Pathways in Rare Events Simulations. *Chem. Phys. Lett.* **2006**, *426*, 168–175.

Graphical TOC Entry